POLITECNICO DI TORINO
Repository ISTITUZIONALE

Controllability and Displacement Analysis of a Three-Link Elastic Microswimmer: A Geometric Control Approach

Original
Controllability and Displacement Analysis of a Three-Link Elastic Microswimmer: A Geometric Control Approach / Attanasi, R., Zoppello, M., Napoli, G.. - In: SIAM JOURNAL ON APPLIED MATHEMATICS. - ISSN 0036-1399. - 86:3(2026), pp. 1035-1057. [10.1137/25M1729538]

Availability:
This version is available at: 11583/3016151 since: 2026-09-30T10:51:49Z

Publisher:
Society for Industrial and Applied Mathematics Publications - SIAM

Published
DOI:10.1137/25M1729538

Terms of use:

This article is made available under terms and conditions as specified in the corresponding bibliographic description in the repository

Publisher copyright

(Article begins on next page)

26 November 2026

CONTROLLABILITY AND DISPLACEMENT ANALYSIS OF A THREE-LINK ELASTIC MICROSWIMMER: A GEOMETRIC CONTROL APPROACH

R. ATTANASI *, M. ZOPPELLO †, AND G. NAPOLI ‡

Abstract. This study investigates the dynamics and controllability of a Purcell three-link microswimmer equipped with passive elastic torsional coils at its joints. By controlling the spontaneous curvature, we analyse the swimmer's motion using both linear and weakly nonlinear approaches. Linear analysis reveals steady harmonic solutions for small-amplitude controls but does not predict any net displacement, whereas weakly nonlinear analysis predicts translation along the orientation of the central link. Using geometric control theory, we prove that the system is small time locally controllable near equilibrium and derive displacement estimates for periodic piecewise constant controls, which are validated through numerical simulations. These findings indicate that oscillatory controls can enable motion in all directions near equilibrium. This work offers foundational insights into the controllability of elastic microswimmers, paving the way for advanced motion planning and control strategies.

Introduction. Microswimmers, especially those inspired by biological systems, have attracted significant attention in recent years because of their potential applications in targeted drug delivery, microscale manipulation, and diagnostic procedures [17, 8]. These miniature robotic swimmers are designed to rely on sophisticated control strategies to navigate viscous environments where traditional propulsion mechanisms are either inefficient or infeasible, as exemplified by the Scallop Theorem [18]. The study of their motion and controllability is crucial for advancing micro-robotic technologies, enhancing their practical applications in medical and industrial fields [20, 15, 4, 7].

A fundamental principle governing the motion of microswimmers is their operation in the very low Reynolds number regime, where inertial effects are negligible. Several basic models of microswimmers have been developed, starting with the three-link swimmer proposed by Purcell [18], followed by the N-link swimmer [1, 13], and systems of coupled microswimmers, as explored in [22, 3]. With regard to the Purcell three-link swimmer, the work of [16] investigated the dynamics and stability of periodic solutions for the joint angles, assuming controlled inputs in the form of periodic torques applied at the joints. However, in many practical scenarios, the shape change of microswimmers occurs passively and is also affected by the elastic response of the swimmer's structure. Some models have studied the continuous bending deformation of elastic flagella with distributed actuation [12], while others introduce a coarse-graining formulation in the asymptotic limit, where small rod-like elements are joined by torsional springs [14]. Notably, previous works such as [15] consider a model where one link is passively elastic and the other actuated periodically, while [20] study a similar elastic microswimmer model primarily via numerical simulations, focusing on displacement analysis without addressing controllability.

This paper introduces and analyzes an *elastic microswimmer*, a variant of the Purcell swimmer in which torsional springs are incorporated at the joints. These springs define a *spontaneous* or *equilibrium* shape for the swimmer, characterized

*Dipartimento di Matematica e Fisica "Ennio De Giorgi", Università del Salento, Lecce, Italy

†Dipartimento di Scienze Matematiche "Giuseppe Luigi Lagrange", Politecnico di Torino, 10129 Torino, Italy

‡ipartimento di Matematica e Applicazioni "Renato Caccioppoli", Università degli Studi di Napoli "Federico II", 80125 Napoli, Italy

This manuscript is for review purposes only.

by specific resting angles. Propulsion emerges from the interplay between internal elastic forces, which drive the swimmer toward its equilibrium shape, and viscous fluid forces, which resist changes in configuration. This physically motivated control paradigm requires only the ability to set the desired resting angles, with the swimmer dynamically evolving toward the prescribed configuration.

A related concept was partially explored in [21], where the authors numerically investigated the complex dynamics of such swimmers, revealing multiple periodic solutions, direction reversals, and bifurcations.

Our analysis begins by linearizing the equations of motion around the straight configuration, which is valid for small deviations in the controlled resting angles. For small-amplitude sinusoidal control gaits, we explicitly integrate the linearized system and demonstrate convergence to a stable periodic trajectory. A subsequent weakly nonlinear analysis shows that these gaits generate net translation along the swimmer's primary axis. The practical relevance of small-amplitude controls is motivated by systems such as electrically actuated hydrogels, where the control field can induce a preferred angular configuration without producing net torque, thus enabling arbitrarily small periodic gaits [5].

A key contribution of this work is the analysis of the microswimmer's maneuverability using tools from geometric control theory. We establish that the system is Small-Time Locally Controllable (STLC), confirming its ability to achieve precise steering near its equilibrium state. Using the Lie bracket formalism, we derive analytical estimates for the swimmer's displacement under both equilibrium and non-equilibrium conditions. This is achieved through piecewise constant control inputs, which mimic the scenario where the lateral links are restricted to two spontaneous configurations. These theoretical predictions are validated through numerical simulations, showing strong agreement between the system's behavior under small sinusoidal gaits and periodic piecewise constant controls. This indicates that displacement estimates obtained from analytically tractable, piecewise constant controls can reliably predict the long-term behavior of systems driven by continuous oscillatory inputs, particularly for short control periods.

The remainder of the paper is organized as follows. Section 1 presents the mathematical model and derives the equations of motion for the three-link elastic microswimmer. Section 2 analyzes the system's response to small-amplitude oscillatory control inputs, comparing the weakly nonlinear solution with full numerical simulations. In Section 3, we first prove the system's STLC properties and then use Lie brackets to estimate displacement, comparing these analytical predictions with numerical results. The Appendices provide supplementary mathematical details and a brief overview of geometric control theory.

1. Model. This section derives the governing equations for a Purcell three-link swimmer, consisting of two lateral links of length L and a central link of length L_0, equipped with torsional springs at the joints (see Figure 1). The aim is to study the motion of the swimmer, controlled by external inputs dictating the desired joint angles. This approach, first introduced in [21], does not directly control the shape angles; instead, it prescribes the target shape that the swimmer should adopt over time. We introduce a Cartesian coordinate system centred at point O. The unit vectors along the x- and y-axes are denoted as $\mathbf{e}_x$ and $\mathbf{e}_y$, respectively. Let $\mathbf{x}$ represent the position vector of the midpoint of the microswimmer's central link. Its Cartesian components are given by $x(t)$ and $y(t)$, such that

$$\mathbf{x}(t) = x(t)\mathbf{e}_x + y(t)\mathbf{e}_y. \tag{1.1}$$

This manuscript is for review purposes only.

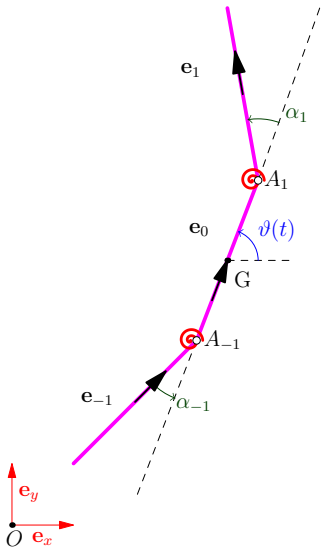

FIG. 1. *Schematic representation of an elastic 3-links microswimmer.*

Finally, let ϑ represent the time-dependent angle between the central link and the positive x-axis. Here, the subscript $j = -1, 0, +1$ denotes the microswimmer links. More precisely, $j = 0$ represents the central link, while $j = -1$ and $j = +1$ represent the lateral links. The orientation of each link is described by the planar unit vectors,

$$\mathbf{e}_j(t) := \cos\varphi_j(t)\mathbf{e}_x + \sin\varphi_j(t)\mathbf{e}_y, \tag{1.2}$$

with

$$\varphi_j(t) := \vartheta(t) + j\alpha_j(t),$$

with $\alpha_{\pm1}$ denoting the alignment angles between adjacent links, as shown in Figure 1. Thus, the triple $x(t), y(t), \vartheta(t)$ describes the position and orientation of the microswimmer in the plane, while the pair $\alpha_{-1}(t), \alpha_{+1}(t)$ defines its shape.

The swimmer's motion is driven by external forces from the fluid's reaction to its shape changes. According to resistive force theory [10], the force and torque exerted by the fluid on each point of a slender body depend solely on the local velocity at that point, neglecting interactions with neighbouring points. Consequently, we can express the force density on the j-th link as

$$\mathbf{f}_j(s,t) = -\xi\, v_{j\parallel}(s,t)\mathbf{e}_j(t) - \eta\, v_{j\perp}(s,t)\mathbf{n}_j(t), \tag{1.3}$$

where $\mathbf{n}_j(t) := \mathbf{e}_z \times \mathbf{e}_j(t)$ and

$$v_{j\parallel}(s,t) := \mathbf{v}_j(s,t)\cdot\mathbf{e}_j(t), \quad v_{j\perp}(s,t) := \mathbf{v}_j(s,t)\cdot\mathbf{n}_j(t), \tag{1.4}$$

represent the longitudinal and transverse components of the velocity, respectively, while ξ and η, whose physical dimensions are $[\mathrm{M}][\mathrm{L}]^{-1}[\mathrm{T}]^{-1}$, denote the positive drag coefficients along the directions $\mathbf{e}_j$ and $\mathbf{n}_j$, respectively. The variable s denotes the arc length parameter measured from the midpoint of a link, such that:

$$s \in \left[-\tfrac{L}{2}, \tfrac{L}{2}\right] \quad \text{if } j = \pm1 \text{ (lateral links)},$$

This manuscript is for review purposes only.

and

$$s \in \left[-\tfrac{L_0}{2}, \tfrac{L_0}{2}\right] \quad \text{if } j = 0 \text{ (central link).}$$

The position of a point on the $j-$th link of the microswimmer can be formulated as

$$\mathbf{x}_j(s,t) = \mathbf{x}(t) + j\frac{L_0}{2}\mathbf{e}_0(t) + \left(s + j\frac{L}{2}\right)\mathbf{e}_j(t),$$

whence

$$\mathbf{v}_j(s,t) = \dot{\mathbf{x}}_j(t) + j\frac{L_0}{2}\dot{\vartheta}(t)\mathbf{n}_0(t) + \left(s + j\frac{L}{2}\right)\dot{\varphi}_j(t)\mathbf{n}_j(t).$$

These equations, together with equations (1.3) and (1.4), can be used to compute the total hydrodynamic force and torque as follows:

$$\mathbf{F}(t) = \sum_{j=\pm 1}\int_{-\frac{L}{2}}^{\frac{L}{2}} \mathbf{f}_j(s,t)\mathrm{d}s + \int_{-\frac{L_0}{2}}^{\frac{L_0}{2}} \mathbf{f}_0(s,t)\mathrm{d}s, \tag{1.5}$$

and

$$\mathbf{M}(t) = \sum_{j=\pm 1}\int_{-\frac{L}{2}}^{\frac{L}{2}} (\mathbf{x}_j(s,t) - \mathbf{x}(t)) \times \mathbf{f}_j(s,t)\mathrm{d}s + \int_{-\frac{L_0}{2}}^{\frac{L_0}{2}} (\mathbf{x}_0(s,t) - \mathbf{x}(t)) \times \mathbf{f}_0(s,t)\mathrm{d}s. \tag{1.6}$$

In the low Reynolds number regime, inertial forces are negligible. Consequently, the two equations governing the swimmer's motion, corresponding to force and torque balance, are

$$\mathbf{F}(t) = \mathbf{0}, \qquad \mathbf{M}(t) = \mathbf{0}. \tag{1.7}$$

Note that these two vector equations, which give three scalar equations, are necessary but not sufficient to fully describe the swimmer's motion, which has five degrees of freedom. Moreover, they do not account for the effects of the torsional springs, which are internal torques exchanged between links of the swimmer and do not contribute to the balance of external forces and torques.

Two additional scalar equations, which do not introduce any new unknowns, are derived from the torque balance on each lateral link at its respective joint. For each of the two links, the total torque includes the hydrodynamic torque acting on the lateral link and the torque exerted by the torsional spring at the joint. Thus, denoting by κ the stiffness of the torsional springs (with physical dimensions $[\mathrm{M}][\mathrm{L}]^2[\mathrm{T}]^{-2}$) we get

$$\mathbf{M}_j(t) = \int_{-\frac{L}{2}}^{\frac{L}{2}} \left(s + j\frac{L}{2}\right)\mathbf{e}_j(t) \times \mathbf{f}_j(s,t)\mathrm{d}s - \kappa\left(\alpha_j(t) - \bar{\alpha}_j\right)\mathbf{e}_z, \quad j = \pm 1 \tag{1.8}$$

where the angles $\bar{\alpha}_j$ denote the *spontaneous alignment angles*, i.e., the angles the swimmer would assume in the absence of external forces. Thus, the presence of torsional springs results in a swimmer shape where $\alpha_j = \bar{\alpha}_j$. A key novelty of this study is considering the angles $\bar{\alpha}_j$ as control gaits.

This manuscript is for review purposes only.

1.1. Dimensionless equations of motion. To non-dimensionalize the equations of motion, we define the characteristic time:

$$\tau_c = \frac{\xi L_0^3}{\kappa},$$

obtained through dimensional analysis by comparing the torque exerted by the coil to the torque exerted by the fluid on swimmer links [16]. Without loss of generality, we use the length of the central link as the characteristic length. All physical quantities are then scaled by their respective characteristic values:

$$x = x^* L_0, \qquad y = y^* L_0, \qquad t = t^* \tau_c \tag{1.9}$$

with forces $\mathbf{F}$ and torques $\mathbf{M}$ scaling as

$$\mathbf{F} = \mathbf{F}^* \left(\frac{\xi L_0^2}{\tau_c} \right), \qquad \mathbf{M} = \mathbf{M}^* \left(\frac{\xi L_0^3}{\tau_c} \right). \tag{1.10}$$

For notational simplicity, we will henceforth omit the asterisk symbol from all quantities. It should be understood that these variables represent scaled dimensionless quantities.

In summary, the dimensionless equations of motion form a system of five scalar equations

$$\begin{cases} \mathbf{e}_x \cdot \mathbf{F}(t) = 0, \\ \mathbf{e}_y \cdot \mathbf{F}(t) = 0, \\ \mathbf{e}_z \cdot \mathbf{M}(t) = 0, \\ \mathbf{e}_z \cdot \mathbf{M}_{-1}(t) = 0, \\ \mathbf{e}_z \cdot \mathbf{M}_{+1}(t) = 0, \end{cases} \tag{1.11}$$

for the five generalized coordinates that define the swimmer's configuration: $x(t)$, $y(t)$, $\vartheta(t)$, $\alpha_{-1}(t)$, $\alpha_{+1}(t)$.

Using equations (1.5) and (1.8) and introducing the state vector

$$\mathbf{y}(t) := [x(t), y(t), \vartheta(t), \alpha_{-1}(t), \alpha_{+1}(t)]^\top,$$

equation (1.11) can be recast in the form:

$$\mathcal{R}(t)\dot{\mathbf{y}}(t) = \mathbf{b}(t), \tag{1.12}$$

where $\mathcal{R}(t)$ is 5×5 symmetric matrix [1], whose entries are detailed for completeness in Appendix A in the case of $L_0 = L$ to obtain a more tractable expression. While $\mathbf{b}(t)$ is:

$$\mathbf{b}(t) = [0, 0, 0, \alpha_{-1}(t) - u_1(t), \alpha_{+1}(t) - u_2(t)]. \tag{1.13}$$

Note that in equation (1.13), u_1 and u_2 denote the angles $\bar{\alpha}_{-1}$ and $\bar{\alpha}_{+1}$, respectively, which will serve as control inputs.

Following [2], since the first two equations of system (1.11) do not depend on $x(t)$ and $y(t)$. This implies that the system is coupled in one direction only, with the orientation variables $\vartheta(t)$, $\alpha_{-1}(t)$ and $\alpha_{+1}(t)$ influencing the translational variables $x(t)$ and $y(t)$, but not vice versa.

This manuscript is for review purposes only.

In fact, the matrix $\mathcal{R}(t)$ can be decomposed into blocks as follows

$$\mathcal{R}(t) = \begin{bmatrix} \mathbf{A} & \mathbf{B} \\ \mathbf{B}^T & \mathbf{C} \end{bmatrix}, \tag{1.14}$$

where $\mathbf{A}$, $\mathbf{B}$ and $\mathbf{C}$ are respectively 2×2, 2×3 and 3×3 matrices, all of which depend only on the variables ϑ, α_{-1} α_{+1}. Thus, the equations of motion can be be decoupled into two subsystems:

$$\begin{bmatrix} \dot{x} \\ \dot{y} \end{bmatrix} = -\mathbf{A}^{-1}\mathbf{B} \begin{bmatrix} \dot{\vartheta} \\ \dot{\alpha}_{-1} \\ \dot{\alpha}_{+1} \end{bmatrix}, \tag{1.15a}$$

$$\left(-\mathbf{B}^\top \mathbf{A}^{-1}\mathbf{B} + \mathbf{C}\right) \begin{bmatrix} \dot{\vartheta} \\ \dot{\alpha}_{-1} \\ \dot{\alpha}_{+1} \end{bmatrix} = \begin{bmatrix} 0 \\ \alpha_{-1} - u_1 \\ \alpha_{+1} - u_2 \end{bmatrix}. \tag{1.15b}$$

This allows us to integrate the equations of motion in two steps. First, we solve system (1.15b), and then use its solutions to solve system (1.15a).

2. Small-amplitude oscillating controls. Inspired by previous research [16, 2], we investigate the motion of a 3-link elastic microswimmer, assuming small oscillating equilibrium angles as control inputs. This allows us to assume consistently small alignment angles and, consequently, linearize the equations of motion for these angles. However, to accurately determine the displacement, we need to consider higher-order approximations of the equations of motion. Despite this, the resulting displacement predictions align well with numerical simulations obtained from the full nonlinear equations of motion. For the numerical solutions, the system of differential equations was integrated using Mathematica's built-in numerical solver. The problem was solved over a specified time interval with zero initial conditions for all state variables. To improve computational efficiency and stability, the solver employed an equation simplification method during the integration process. Furthermore, they are consistent with the findings of [21].

2.1. Linear analysis. To facilitate analytical computations, from now on we concentrate on the case of all links of equal length L. We consider the equilibrium point $((\vartheta, \alpha_{-1}, \alpha_{+1}), (u_1, u_2)) = ((\vartheta_0, 0, 0), (0, 0))$ and assume small-amplitude periodic control gaits

$$u_1(t) = \epsilon \sin(\omega t), \qquad u_2(t) = \epsilon \sin(\omega t + \phi), \tag{2.1}$$

with $\epsilon \ll 1$ the dimensionless amplitude, ω the dimensionless frequency, and ϕ a shift phase.

Consistently, we assume the unknown variables can be expanded in a power series of ϵ around the equilibrium point, as done in [2, 16]:

$$x(t) = \sum_{k=1}^{\infty} \epsilon^k x^{(k)}(t), \quad y(t) = \sum_{k=1}^{\infty} \epsilon^k y^{(k)}(t), \tag{2.2a}$$

$$\vartheta(t) = \vartheta_0 + \sum_{k=1}^{\infty} \epsilon^k \vartheta^{(k)}(t), \quad \alpha_{\pm 1}(t) = \sum_{k=1}^{\infty} \epsilon^k \alpha_{\pm 1}^{(k)}(t). \tag{2.2b}$$

This manuscript is for review purposes only.

Note that the power series for $\alpha_{\pm 1}(t)$ starts at order $O(\epsilon)$, since the expansion is performed around the equilibrium point $(\alpha_{-1}, \alpha_{+1}) = (0, 0)$, which implies that the zeroth-order term vanishes.

Replacing equations (2.2) into (1.15b), $O(\epsilon)$ we obtain

$$\begin{bmatrix} \dot{\vartheta}^{(1)} \\ \dot{\alpha}_{-1}^{(1)} \\ \dot{\alpha}_{+1}^{(1)} \end{bmatrix} = \nu \begin{bmatrix} d & c & c \\ c & a & b \\ c & b & a \end{bmatrix} \begin{bmatrix} 0 \\ \alpha_{-1}^{(1)} - \sin(\omega t) \\ \alpha_{+1}^{(1)} - \sin(\omega t + \phi) \end{bmatrix}, \tag{2.3}$$

where $\nu = \xi/\eta$, $a = -96/5$, $b = -66/5$, $c = 42/5$ and $d = -24/5$.

Solving the system (2.3), we get

$$\vartheta^{(1)}(t) = c_3 + \frac{c(c_1 + c_2)}{a+b}\left(\mathrm{e}^{(a+b)\nu t} - 1\right) + \frac{2c\nu}{\nu^2(a+b)^2 + \omega^2} \times \\ \times \left(\nu(a+b)\sin\left(\omega t + \frac{\phi}{2}\right) + \omega\cos\left(\omega t + \frac{\phi}{2}\right)\right)\cos\left(\frac{\phi}{2}\right), \tag{2.4a}$$

$$\alpha_{-1}^{(1)}(t) = \mathrm{e}^{a\nu t}\left(c_1\cosh(b\nu t) + c_2\sinh(b\nu t)\right) + \\ + q_1\cos(\omega t) + q_2\cos(\omega t + \phi) + q_3\sin(\omega t) + q_4\sin(\omega t + \phi), \tag{2.4b}$$

$$\alpha_{+1}^{(1)}(t) = \mathrm{e}^{a\nu t}\left(c_1\sinh(b\nu t) + c_2\cos(b\nu t)\right) + \\ + q_1\cos(\omega t + \phi) + q_2\cos(\omega t) + q_3\sin(\omega t + \phi) + q_4\sin(\omega t), \tag{2.4c}$$

where c_i, $i = 1, 2, 3$, are integration constants, and

$$q_1 = \frac{a\nu\omega\left(\nu^2(a^2 - b^2) + \omega^2\right)}{\nu^4\left(a^2 - b^2\right)^2 + 2\nu^2\omega^2\left(a^2 + b^2\right) + \omega^4},$$

$$q_2 = \frac{b\nu\omega\left(\nu^2\left(b^2 - a^2\right) + \omega^2\right)}{\nu^4\left(a^2 - b^2\right)^2 + 2\nu^2\omega^2\left(a^2 + b^2\right) + \omega^4},$$

$$q_3 = \frac{\nu^4\left(a^2 - b^2\right)^2 + \nu^2\omega^2\left(a^2 + b^2\right)}{\nu^4\left(a^2 - b^2\right)^2 + 2\nu^2\omega^2\left(a^2 + b^2\right) + \omega^4},$$

$$q_4 = \frac{2ab\nu^2\omega^2}{\nu^4\left(a^2 - b^2\right)^2 + 2\nu^2\omega^2\left(a^2 + b^2\right) + \omega^4}.$$

Expanding equation (1.15a) to first order in ϵ yields

$$\begin{bmatrix} \dot{x}^{(1)} \\ \dot{y}^{(1)} \end{bmatrix} = \frac{1}{6}\begin{pmatrix} 0 & -\sin\vartheta_0 & \sin\vartheta_0 \\ 0 & \cos\vartheta_0 & -\cos\vartheta_0 \end{pmatrix} \begin{bmatrix} \dot{\vartheta}^{(1)} \\ \dot{\alpha}_{-1}^{(1)} \\ \dot{\alpha}_{+1}^{(1)} \end{bmatrix}, \tag{2.5}$$

which easily lead to

$$x^{(1)}(t) = \frac{\alpha_{+1} - \alpha_{-1}}{6}\sin\vartheta_0, \qquad y^{(1)}(t) = \frac{\alpha_{-1} - \alpha_{+1}}{6}\cos\vartheta_0, \tag{2.6}$$

These equations indicate that, to leading order, the trajectory of the centre of the central link is orthogonal to the link's direction. Note that, in equations (2.4b) and (2.4c), a and b are both negative with $a < b$. This implies that the part of the solution involving arbitrary constants is damped. Consequently, for sufficiently long times, only the periodic solution persists. As a result, the trajectory described by equations (2.6) also becomes periodic for sufficiently long times, resulting in no net advancement of the swimmer.

This manuscript is for review purposes only.

2.2. Weakly nonlinear analysis. To determine whether the swimmer experiences net displacement under the influence of small-amplitude oscillating controls, it is essential to analyse higher-order terms in the perturbation expansion.

We first consider equation (1.15b) that, at $O(\epsilon^2)$, leads to the linear homogeneous system

$$\begin{bmatrix} \dot{\vartheta}^{(2)} \\ \dot{\alpha}_{-1}^{(2)} \\ \dot{\alpha}_{+1}^{(2)} \end{bmatrix} = \nu \begin{bmatrix} 0 & c & c \\ 0 & a & b \\ 0 & b & a \end{bmatrix} \begin{bmatrix} \vartheta^{(2)} \\ \alpha_{-1}^{(2)} \\ \alpha_{+1}^{(2)} \end{bmatrix} \tag{2.7}$$

whose admit only the damped solution. However, when it is solved with null initial conditions, it gives the trivial solution

$$\vartheta^{(2)}(t) = 0, \qquad \alpha_{-1}^{(2)}(t) = 0, \qquad \alpha_{+1}^{(2)}(t) = 0. \tag{2.8}$$

This implies that, to order $O(\epsilon^2)$, the right-hand side of equation (1.15a) depends only on the variables $\vartheta^{(1)}, \alpha_{-1}^{(1)}, \alpha_{+1}^{(1)}$:

$$\begin{bmatrix} \dot{x}^{(2)} \\ \dot{y}^{(2)} \end{bmatrix} = (a_{11}\dot{\vartheta}^{(1)} + a_{12}\dot{\alpha}_{-1}^{(1)} + a_{13}\dot{\alpha}_{+1}^{(1)}) \begin{bmatrix} \cos\vartheta_0 \\ \sin\vartheta_0 \end{bmatrix}, \tag{2.9}$$

where

$$a_{11} := \frac{(\nu-2)(\alpha_{-1}^{(1)} - \alpha_{+1}^{(1)})}{6\nu}, \quad a_{12} := -\frac{(2+\nu)\alpha_{-1}^{(1)} + (\nu-1)\alpha_{+1}^{(1)} + 3\nu\vartheta^{(1)}}{18\nu},$$

$$a_{13} := \frac{(\nu-1)\alpha_{-1}^{(1)} + (2+\nu)\alpha_{+1}^{(1)} + 3\nu\vartheta^{(1)}}{18\nu}.$$

Unfortunately, due to the nonlinear nature of system (2.9), an exact analytical solution cannot be obtained. However, following the approach described in [2], we can focus on the long-term behaviour and compute the net displacement of the microswimmer over one period. Thus, by substituting the periodic components of the solutions (2.4a-2.4c) into equation (2.9) and integrating over a period $T = 2\pi/\omega$, we obtain:

$$\begin{bmatrix} \Delta x^{(2)} \\ \Delta y^{(2)} \end{bmatrix} = \frac{60\pi(\nu-1)\nu\left(972\nu^2 + 5\omega^2\right)\sin\phi}{\left(36\nu^2+\omega^2\right)\left(26244\nu^2+25\omega^2\right)} \begin{bmatrix} \cos\vartheta_0 \\ \sin\vartheta_0 \end{bmatrix}.$$

The magnitude of the displacement after one period of the periodic solution is:

$$\Delta^{(2)} = \sqrt{(\Delta x^{(2)})^2 + (\Delta y^{(2)})^2}, \tag{2.10}$$

whence we obtain

$$\Delta^{(2)} = \frac{60\pi\nu\left(972\nu^2 + 5\omega^2\right)(1-\nu)|\sin\phi|}{\left(36\nu^2+\omega^2\right)\left(26244\nu^2+25\omega^2\right)}, \tag{2.11}$$

along the ϑ_0 direction. The maximum displacement is achieved for a phase shift of $\phi = \pm\pi/2$. Moreover, opposite signs of ϕ correspond to opposite directions of the microswimmer's motion.

REMARK 1. *We note that if $\nu = 1$, the system experiences no net displacement, since $\Delta^{(2)} = 0$. This is well known in the literature [9]; for isotropic drag coefficients, the resulting thrust on the swimmer is zero. Furthermore, the net displacement also vanishes in the limit $\nu \to 0$, which corresponds to the case where the orthogonal drag coefficient is much larger than the parallel one, effectively preventing motion.*

This manuscript is for review purposes only.

2.3. Asymptotic leading order solution. Below we summarize the long-term solutions obtained in the previous sections, for the case where all links have equal length.. Since the maximum displacement over a period occurs for $\phi = \pm\pi/2$, we fix $\phi = \pi/2$. The asymptotic motion of the centre of the central link is obtained by combining the periodic parts of the solutions (2.6) and (2.9), obtaining:

$$\begin{bmatrix} x^{\infty}(t) \\ y^{\infty}(t) \end{bmatrix} = \epsilon\sigma^{(1)}(t) \begin{bmatrix} -\sin\vartheta_0 \\ \cos\vartheta_0 \end{bmatrix} + \epsilon^2\sigma^{(2)}(t) \begin{bmatrix} \cos\vartheta_0 \\ \sin\vartheta_0 \end{bmatrix}, \tag{2.12}$$

where

$$\sigma^{(1)}(t) = \frac{\nu((\omega - 6\nu)\sin(\omega t) + (6\nu + \omega)\cos(\omega t))}{36\nu^2 + \omega^2}, \tag{2.13}$$

$$\begin{aligned} \sigma^{(2)}(t) = &\frac{1}{(36\nu^2 + \omega^2)\,(26244\nu^2 + 25\omega^2)} \Big(6\nu(5(\nu - 1)t\omega(972\nu^2 + 5\omega^2)) + \\ &(9\nu + 4)\left(\left(5\omega^2 - 972\nu^2\right)\sin^2(\omega t) + 96\nu\omega\sin(2\omega t)\right) \Big). \end{aligned} \tag{2.14}$$

This analysis reveals that the motion consists of two components: a primary periodic component orthogonal to the central link and a secondary component parallel to the link. Only the latter contributes to the net advancement of the swimmer over a period. As a result, the microswimmer undergoes large periodic transverse motions in order to achieve a small forward displacement.

Furthermore, throughout this phase, the direction of the central link fluctuates around its initial orientation:

$$\vartheta^{\infty}(t) = \vartheta_0 - \epsilon\frac{42\nu((162\nu + 5\omega)\sin(\omega t) + (162\nu - 5\omega)\cos(\omega t))}{26244\nu^2 + 25\omega^2}. \tag{2.15}$$

while the lateral links oscillate around the the strait configuration

$$\begin{aligned} \alpha^{\infty}_{-1}(t) = \frac{\epsilon}{D}\Big(&6\nu((157464\nu^3 - 10692\nu^2\omega + 2262\nu\omega^2 + 55\omega^3)\sin(\omega t) - \\ &16\omega\left(972\nu^2 - 132\nu\omega + 5\omega^2\right)\cos(\omega t)) \Big), \end{aligned} \tag{2.16}$$

$$\begin{aligned} \alpha^{\infty}_{+1}(t) = \frac{\epsilon}{D}\Big(&6\nu(16\omega\left(972\nu^2 + 132\nu\omega + 5\omega^2\right)\sin(\omega t) + \\ &\left(157464\nu^3 + 10692\nu^2\omega + 2262\nu\omega^2 - 55\omega^3\right)\cos(\omega t)) \Big), \end{aligned} \tag{2.17}$$

where,

$$D := 944784\nu^4 + 27144\nu^2\omega^2 + 25\omega^4.$$

In conclusion, our analysis shows that the solutions for the shape angles rapidly converge to a closed loop, corresponding to a periodic motion. Consequently, the swimmer's orientation also approaches a harmonic solution, with corrections appearing at least at order ϵ^3. This implies that, on average, the swimmer moves along a straight trajectory determined by the initial orientation of the central link, without any net rotation.

This manuscript is for review purposes only.

As for the swimmer's position, the variables $x(t)$ and $y(t)$ exhibit a similar pattern: at $O(\epsilon)$, their solutions converge to harmonic motions. However, corrections at $O(\epsilon^2)$ reveal that the microswimmer experiences a net displacement over a cycle, even though the other variables follow closed loops.

Swimmer trajectories are shown in Figure 3, $\vartheta(t)$ and the shape angles trajectories in Figure 4. The asymptotic harmonic solution is compared with the results of numerical simulations of the nonlinear model for various values of the amplitude ϵ. The asymptotic approximation proves to be highly satisfactory, even for relatively large values of the parameter ϵ.

REMARK 2. *The analysis in this section was performed for a swimmer consisting of three links of equal length L. However, similar behavior is observed when the Purcell swimmer has lateral arms (i.e., the links along the directions $\mathbf{e}_{-1}$ and $\mathbf{e}_1$) of length L, while the central link has a different length L_0. Due to the swimmer's symmetry, it still translates along the direction of the central link (ϑ_0). Furthermore, the orientation and shape variables continue to converge to a closed loop (see Figures 6 and 7). For completeness, we also report the expression for the displacement $\Delta^{(2)}$ in this case, analogous to equation (2.11):*

$$\Delta^{(2)} = \frac{4\lambda(4+\lambda)(1+2\lambda)\pi(1-\nu)\nu\left[36\lambda^2(8+12\lambda+7\lambda^2)\nu^2+5\omega^2\right]|\sin\phi|}{(36\lambda^4\nu^2+\omega^2)\left[36(8+12\lambda+7\lambda^2)^2\nu^2+25\omega^2\right]}, \tag{2.18}$$

where $\lambda = L_0/L$. As in the case of equal link lengths, the maximum displacement occurs for a phase shift $\phi = \pm\pi/2$. As noted in Remark 1, the net displacement is zero when $\nu = 1$ or in the limit $\nu \to 0$.

2.4. Comparison with numerical simulations. The quasi-linear approximation captures only the leading-order motion of the swimmer with respect to the input amplitude ϵ. To assess the accuracy of this approximation, we will compare certain asymptotic quantities with those obtained from numerical solutions of the nonlinear equations. The parameters used for all numerical integrations performed in this section are $\nu = \frac{1}{2}$ and $\vartheta_0 = 0$ with $\phi = \frac{\pi}{2}$.

A key quantity to compare, which helps us determine the microswimmer's performance as a function of frequency, is the average speed in the harmonic regime, given by

$$\bar{v} = \frac{\omega\,\epsilon^2\Delta^{(2)}}{2\pi}. \tag{2.19}$$

This is obtained by integrating equation (2.18) over a single period and dividing by the period length.

The average speed attains its maximum value at:

$$\omega_{\text{opt}} = \pm 18\sqrt{\frac{3}{5}}\nu, \tag{2.20}$$

where it assumes the value:

$$\bar{v}_{\max} = \frac{15\sqrt{15}}{512}(1-\nu)\,\epsilon^2. \tag{2.21}$$

Figure 2 (left) presents a comparison between the numerical solution of the full nonlinear problem and the analytical expression given by equation (2.19). The numerical

This manuscript is for review purposes only.

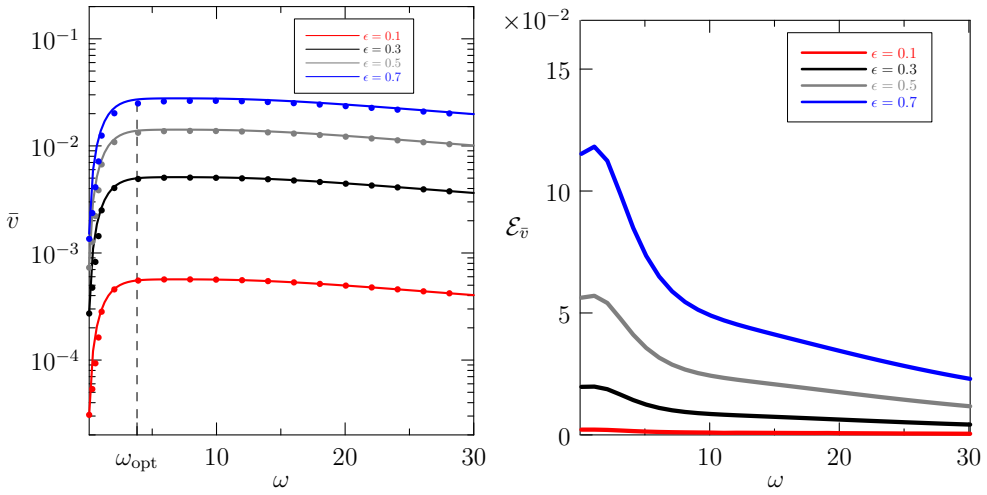

FIG. 2. *(Left) Plots of $\bar{v}$ versus frequency ω, are shown for $\varepsilon = 0.1, 0.3, 0.5, 0.7$. Both theoretical results (solid lines) and numerical results (dotted lines) are included. (Right) The relative error of the mean velocity, $\mathcal{E}_{\bar{v}}$, quantifies the discrepancy between the theoretical and the numerical results.*

value was calculated considering the long-time solution, i.e., in the harmonic regime, and averaging over 100 periods. The use of a large number of periods is particularly important for low frequencies, where the definition of average velocity can be unreliable due to significant fluctuations in displacement over a single period. Averaging over many periods mitigates this discrepancy. Figure 2 (right) illustrates the trend of the relative error $\mathcal{E}_{\bar{v}}$

$$\mathcal{E}_{\bar{v}} = \frac{|\bar{v} - \bar{v}^{\text{num}}|}{|\bar{v}^{\text{num}}|},$$

as a function of frequency ω, for several values of the amplitude actuation ϵ. In the following, we present a comparison between the results of numerical integration of the fully non-linear system and the theoretical predictions obtained from linear and weakly non-linear analyses. For these simulations, we set $\omega = \omega_{\text{opt}}$.

Figure 3 illustrates the trajectory of the studied microswimmer in the $x - y$ plane. To explore the effect of varying control amplitudes, the trajectory is plotted for different values of the actuation amplitude ϵ. For $\epsilon = 0.1$, the plot shows the first two periods of integration. For $\epsilon = 0.5$, both trajectories are plotted from $t = 4\pi/\omega$, while for $\epsilon = 0.7$, both trajectories are plotted starting at $t = 6\pi/\omega$. This choice was made to ensure that the different trajectories are clearly distinguishable within the same figure. The close alignment between these two sets of results demonstrates excellent agreement, thereby validating the theoretical approach.

ω	L	ξ	η	ϑ_o
$6.97\,\text{s}^{-1}$	$1\,\mu$m	$1\,\text{Ns}/\mu\text{m}^2$	$2\,\text{Ns}/\mu\text{m}^2$	0 rad

TABLE 1

Values of the parameters used in the numerical simulations for 3-links microswimmer with equal links.

This manuscript is for review purposes only.

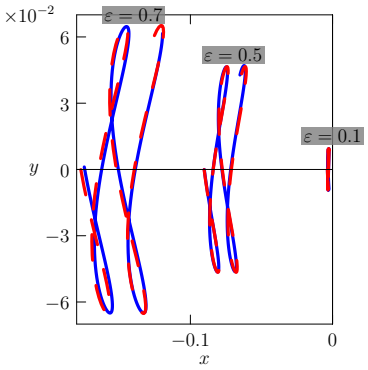

FIG. 3. *Trajectories in the $x - y$ plane for different values of ϵ. Solid blue lines represent the numerical solutions of the fully nonlinear equations of motion, while dashed red lines represent solutions obtained from the weak nonlinear analysis. Parametrs are that shown in Table 1.*

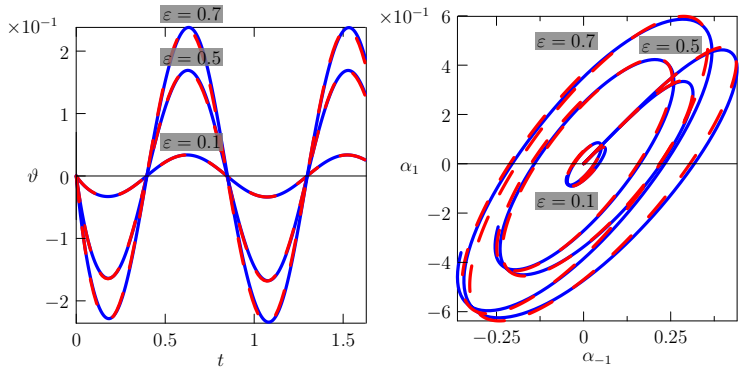

FIG. 4. *Orientation angle ϑ as a function of time (left) and parametric plot of the shape angles in the $\alpha_{-1} - \alpha_{+1}$ plane (right), are shown for several values of the amplitude control gaits ϵ. Solid blue lines represent the numerical solutions of the full nonlinear equations of motion, while dashed red lines represent solutions obtained from linear analysis. Parametrs are that shown in Table 1.*

Moreover, the numerical results exhibit excellent agreement with our asymptotic theoretical predictions for the variables $\vartheta(t)$ and $\alpha_{\pm 1}(t)$. As shown in Figure 4, the dashed red lines, representing the theoretical predictions, closely follow the blue lines, which depict the curves obtained from numerical integration.

2.4.1. Case of unequal link lengths. The simulations presented in this section consider a swimmer with equal-length links, i.e., $\lambda = 1$. Here, we provide the expressions for the optimal frequency and optimal speed for the case of an arbitrary λ.

The optimal frequency is given by:

$$\omega_{\text{opt}} = \pm \frac{3\nu\sqrt{\lambda^2(8 + 12\lambda + 7\lambda^2)}}{\sqrt{5}}, \tag{2.22}$$

and the corresponding maximal speed is:

$$\bar{v}_{\max} = \frac{\sqrt{5}\pi^2\lambda(4+\lambda)(1+2\lambda)(1-\nu)\sqrt{\lambda^2(8+12\lambda+7\lambda^2)\nu^2}}{(24(2+3\lambda+3\lambda^2)^2\nu)}. \tag{2.23}$$

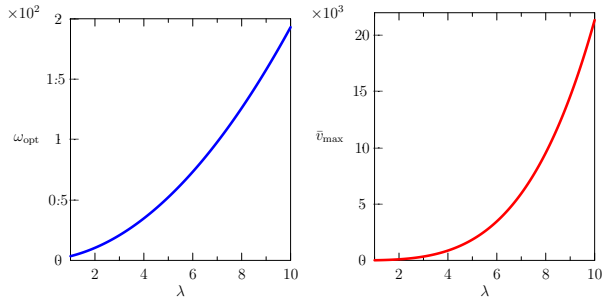

FIG. 5. *Plots of the optimal frequency ω_{opt} and of the maximal velocity $\bar{v}_{\max}$ as a function of the ratio λ, as shown in Equations (2.22) and (2.23). Here ν is equal to $1/2$.*

From Figures 5, it is clear that both the maximum speed and the optimal frequency ω_{opt} increase monotonically with λ. In other words, the smaller the lateral links are relative to the central link, the higher the optimal beating frequency and the corresponding maximum speed. Since these numerical simulations indicate that there is no specific value of λ that maximizes displacement, setting $\lambda = 1$ in the theoretical analysis is not restrictive.

It is also worth noting that the qualitative behavior of the trajectories remains essentially the same for both equal and unequal link lengths. This can be seen by comparing Figure 3 with Figure 6, as well as Figure 4 with Figure 7. Therefore, the link lengths do not alter the fundamental nature of the motion: the swimmer consistently translates along the direction of the central link, while the orientation and shape variables converge to periodic solutions in both cases.

ω	L	L_0	ξ	η	ϑ_o
$6\sqrt{3}\,\text{s}^{-1}$	$1\,\mu\text{m}$	$2\mu\text{m}$	$1\,\text{Ns}/\mu\text{m}^2$	$2\,\text{Ns}/\mu\text{m}^2$	0 rad

TABLE 2
Values of the parameters used in the numerical simulations.

3. Small-Time Local Controllability. Linearisation around the equilibrium point provides valuable insights into the system's dynamics, revealing that the orientation and shape angles converge to steady periodic solutions with short periods over extended time intervals. Furthermore, the linear analysis indicates that the system exhibits translational behaviour in the direction of ϑ. Building upon this understanding, we now aim to investigate the controllability of the system, specifically determining whether it can be steered to any desired point within a neighbourhood of the equilibrium.

Returning to equation of motion (1.12) and noting that $\mathcal{R}$ is invertible [1], we can define:

$$\mathbf{q}_0(\mathbf{y}) := \mathcal{R}^{-1}(t)[0,0,0,\alpha_{-1}(t),\alpha_{+1}(t)]^\top,$$

$$\mathbf{q}_1(\mathbf{y}) := \mathcal{R}^{-1}(t)[0,0,0,-1,0]^\top, \quad \mathbf{q}_2(\mathbf{y}) := \mathcal{R}^{-1}(t)[0,0,0,0,-1]^\top,$$

and rewrite the equations of motion as a nonlinear affine control system with drift:

$$\dot{\mathbf{y}} = \mathbf{q}_0(\mathbf{y}) + \sum_{k=1}^{2} u_k \mathbf{q}_k(\mathbf{y}), \tag{3.1}$$

This manuscript is for review purposes only.

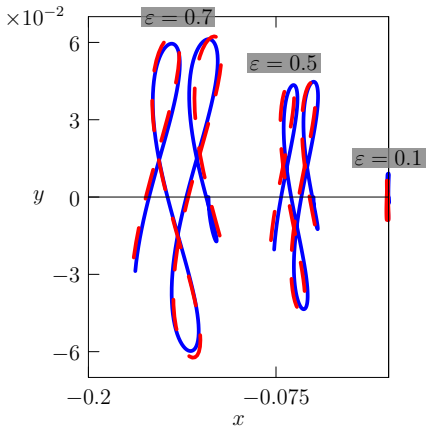

FIG. 6. *Trajectories in the $x-y$ plane for different values of ϵ for a microswimmer composed of two lateral links of length $L=1$ each and a central link of length $2L$. Solid blue lines represent the numerical solutions of the fully nonlinear equations of motion, while dashed red lines represent solutions obtained from the weak nonlinear analysis. Parametrs are that shown in Table 2.*

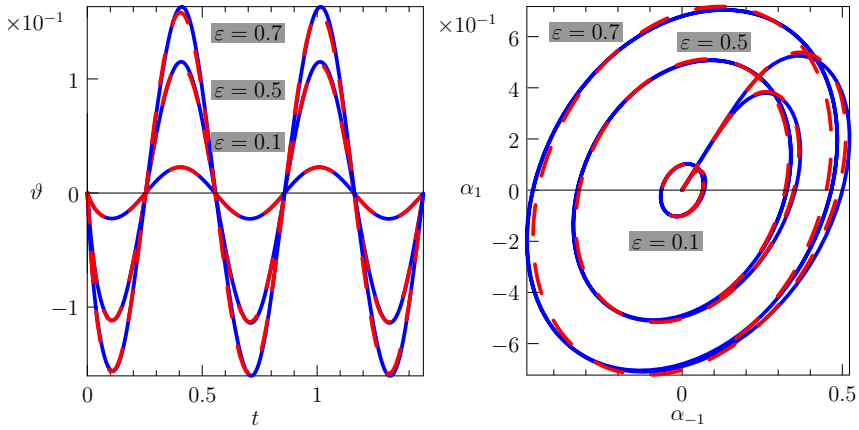

FIG. 7. *Orientation angle ϑ as a function of time (left) and parametric plot of the shape angles in the $\alpha_{-1}-\alpha_{+1}$ plane (right), are shown for several values of the amplitude control gaits ϵ for a microswimmer with links having different lengths. In particular in these numerical simulations we choose the length of the external arms $L=1$ and the length of the central link $L_0=2$. Solid blue lines represent the numerical solutions of the full nonlinear equations of motion, while dashed red lines represent solutions obtained from linear analysis. Parametrs are that shown in Table 2.*

with control gaits $u_k(t)$.

The study of controllability for nonlinear affine control systems, as defined by equation (3.1), is challenging due to their inherent nonlinearity. Therefore, we will focus on small-time local controllability. To this end, we will require several concepts from geometric control theory, including the definition of small-time local controllability itself. For a more detailed discussion, we refer the reader to Coron's book [6]. However, we will provide a concise summary of the relevant definitions and theorems in Appendix B.

3.1. STLC of the elastic microswimmer. To demonstrate the small-time local controllability of system (3.1) with $u_1(t) \neq u_2(t)$ for $t \geq 0$, we consider the equi-

This manuscript is for review purposes only.

librium point $(\mathbf{y}_e, \mathbf{u}_e)$, where $\mathbf{y}_e = [x, y, \vartheta_0, 0, 0]$ and $\mathbf{u}_e = [0, 0]$, corresponding to a straight microswimmer. We will employ Sussmann's condition to verify controllability.

THEOREM 3.1. *System (3.1) is small time locally controllable around equilibrium points* $(\mathbf{y}_e, \mathbf{u}_e) = ((x, y, \vartheta_0, 0, 0), (0, 0))$.

proof The proof relies on Sussmann's condition and Theorem B.1 in Appendix B.

First, we consider the Lie algebra generated by the vector fields, $\mathrm{Lie}(\{\mathbf{q}_0, \mathbf{q}_1, \mathbf{q}_2\})$. The Lie algebra rank condition requires that the Lie brackets of these vector fields span the entire tangent space at the equilibrium point. To verify this, we define the following vector fields:

$$\mathbf{g}_1(\mathbf{y}_e) = \mathbf{q}_1(\mathbf{y}_e), \quad \mathbf{g}_2(\mathbf{y}_e) = \mathbf{q}_2(\mathbf{y}_e), \quad \mathbf{g}_3(\mathbf{y}_e) = [\mathbf{q}_1, \mathbf{q}_2](\mathbf{y}_e),$$

$$\mathbf{g}_4(\mathbf{y}_e) = [\mathbf{q}_1, [\mathbf{q}_1, \mathbf{q}_2]](\mathbf{y}_e), \quad \mathbf{g}_5(\mathbf{y}_e) = [\mathbf{q}_2, [\mathbf{q}_1, \mathbf{q}_2]](\mathbf{y}_e).$$

By calculating the explicit expressions for these vector fields, we can explicitly build the matrix $\mathbf{L} = (\mathbf{g}_1, \mathbf{g}_2, \mathbf{g}_3, \mathbf{g}_4, \mathbf{g}_5)$:

$$\mathbf{L}(\mathbf{y}_e) = -\nu \begin{bmatrix} \sin\vartheta_0 & -\cos\vartheta_0 & c & a & b \\ -\sin\vartheta_0 & \cos\vartheta_0 & c & b & a \\ 12(\nu-1)\cos\vartheta_0 & 12(\nu-1)\sin\vartheta_0 & 0 & 0 & 0 \\ -\nu l_a \sin\vartheta_0 & \nu l_a \cos\vartheta_0 & -\nu l_b & -\nu l_c & \nu l_d \\ -\nu l_a \sin\vartheta_0 & \nu l_a \cos\vartheta_0 & -\nu l_b & -\nu l_d & \nu l_c \end{bmatrix}, \tag{3.2}$$

where

$$l_a := \frac{57}{7}c - \frac{21}{5}a\nu - 54d\nu^2, \qquad l_b := -\frac{18}{5}b + \frac{3}{2}ab\nu^2, \tag{3.3a}$$

$$l_c := -9a + \frac{3}{2}ab\nu + 3ad\nu^2, \qquad l_d := -\frac{39}{4}cd + 3ad\nu + \frac{183}{4}d^2\nu^2. \tag{3.3b}$$

Since $\det \mathbf{L}$ vanishes at the real values $\eta/\xi = 1$ and $\eta/\xi = -45/19$, that are not physically relevant for slender swimmers since $\eta/\xi > 1$, we conclude that $\mathbf{L}$ has full rank. Hence, the vectors $\mathbf{g}_i$ span the entire space $\mathbb{R}^5$, satisfying the Lie algebra rank condition.

To demonstrate that the Sussmann condition holds for all $\Lambda \in [0, 1]$, consider a generic element $\mathbf{h} \in \mathrm{Br}(\{\mathbf{q}_0, \mathbf{q}_1, \mathbf{q}_2\})$. We must select $\mathbf{h}$ such that $\delta_0(\mathbf{h})$ is odd and $\delta_i(\mathbf{h})$ is even for $i = 1, 2$.

The minimum total degree, denoted by d, for which such brackets exist is $d = 3$. When $d = 1$, the Sussmann condition trivially holds for all Λ by choosing $\mathbf{g} = \mathbf{q}_1$ or $\mathbf{g} = \mathbf{q}_2$.

For brackets of degree $d = 3$, where $\mathbf{q}_0$ appears an odd number of times and other $\mathbf{q}_k$ appear an even number of times, $\mathbf{h}$ must take the form:

$$\mathbf{h} = [\mathbf{q}_k, [\mathbf{q}_k, \mathbf{q}_0]], \tag{3.4}$$

for $k = 1, 2$.

Since it can be explicitly verified that $[\mathbf{q}_1, [\mathbf{q}_1, \mathbf{q}_0]](\mathbf{y}_e) = -[\mathbf{q}_2, [\mathbf{q}_2, \mathbf{q}_0]](\mathbf{y}_e)$, we obtain

$$\sigma(\mathbf{h})(\mathbf{y}_e) = [\mathbf{q}_1, [\mathbf{q}_1, \mathbf{q}_0]](\mathbf{y}_e) + [\mathbf{q}_2, [\mathbf{q}_2, \mathbf{q}_0]](\mathbf{y}_e) = \mathbf{0}.$$

This manuscript is for review purposes only.

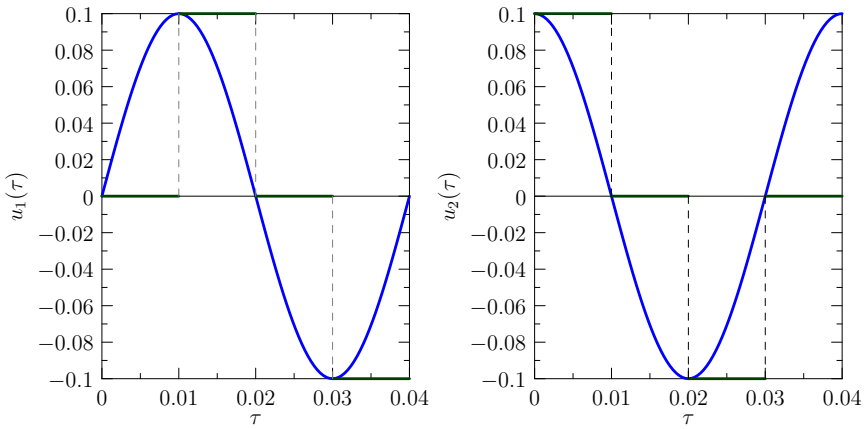

FIG. 8. *Continuous inputs with $\epsilon = 0.1$ and their approximation with piecewise constant functions.*

This implies that $\sigma(\mathbf{h})(\mathbf{y}_e)$ lies in the span of $\mathbf{g}_1(\mathbf{y}_e)$. Since:

$$1 = \Lambda\delta_0(\mathbf{g}_1) + \sum_{k=1}^{2}\delta_k(\mathbf{g}_1) < \Lambda\delta_0(\mathbf{h}) + \sum_{k=1}^{2}\delta_k(\mathbf{h}) = \Lambda + 2, \quad \forall\Lambda \geq 0, \tag{3.5}$$

the Sussmann condition is satisfied for all $\Lambda \in [0, 1]$. Therefore, by Theorem B.1, the system is small-time locally controllable.

REMARK 3. *For iterated Lie brackets of degree greater than 3, verifying the Sussmann condition is unnecessary. This is because the Lie algebra rank condition, satisfied by vector fields of order up to 3, guarantees that higher-order brackets can be expressed as linear combinations of lower-order brackets. Consequently, $\sigma(\mathbf{h})$ also lies within the span of these lower-order brackets.*

3.2. Displacement approximation with piecewise constant controls. After establishing small-time local controllability, we now turn to approximating the system's displacement using piecewise constant controls. These controls are particularly well-suited for capturing system behavior, especially over short time intervals, within the framework of geometric control theory.

Consider a small time interval $\tau > 0$ and a constant $\gamma > 0$. We define the following piecewise constant control inputs:

$$u_1(t) = \begin{cases} 0, & 0 \leq t \leq \tau, \\ \gamma, & \tau < t \leq 2\tau, \\ 0, & 2\tau < t \leq 3\tau, \\ -\gamma, & 3\tau < t \leq 4\tau. \end{cases} \qquad u_2(t) = \begin{cases} \gamma, & 0 \leq t \leq \tau, \\ 0, & \tau < t \leq 2\tau, \\ -\gamma, & 2\tau < t \leq 3\tau, \\ 0, & 3\tau < t \leq 4\tau. \end{cases} \tag{3.6}$$

These control gaits, depicted in Figure 8, describe a periodic cycle of the swimmer's strokes, comprising four distinct phases. In each phase, the swimmer propels itself by activating only one of the two side links. A desired spontaneous configuration is assigned to each phase, which activates the torsional springs to push the link towards this configuration.

This manuscript is for review purposes only.

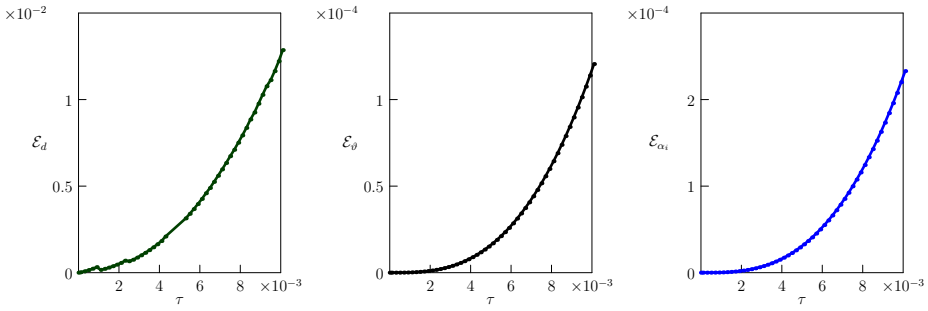

FIG. 9. *Relative error of the x-component defined as* $\mathcal{E}_x := \frac{|x(4\tau) - x^{num}(4\tau)|}{|x^{num}(4\tau)|}$, $\mathcal{E}_\vartheta := \frac{|\vartheta(4\tau) - \vartheta^{num}(4\tau)|}{|\vartheta^{num}(4\tau)|}$, $\mathcal{E}_{\alpha_i} := \frac{|\alpha_i(4\tau) - \alpha_i^{num}(4\tau)|}{|\alpha_i^{num}(4\tau)|}$, *respectively. Parametrs are that shown in Table 1.*

The variation of the state vector after one cycle is given by:

$$\mathbf{y}(4\tau) = \mathbf{y}_0 + 4\tau\mathbf{q}_0|_{\mathbf{y}_0} + \tau^2\left(6(\nabla\mathbf{q}_0\cdot\mathbf{q}_0) + 2\gamma[\mathbf{q}_1,\mathbf{q}_0]\right. \\ \left. +2\gamma[\mathbf{q}_2,\mathbf{q}_0] - \gamma^2[\mathbf{q}_1,\mathbf{q}_2]\right)_{\mathbf{y}_0} + o(\tau^2). \tag{3.7}$$

Considering the initial condition $\mathbf{y}_0 = \mathbf{y}_e$ and recalling that $\mathbf{q}_0(\mathbf{y}_e) = \mathbf{0}$, we obtain:

$$\mathbf{y}(4\tau) = 12\gamma\nu\tau^2\Big(\gamma(1-\nu)\cos\vartheta, \gamma(1-\nu)\sin\vartheta, \\ \frac{2268\nu}{25}, -\frac{4374\nu}{25}, -\frac{4374\nu}{25}\Big) + o(\tau^2). \tag{3.8}$$

Consequently, the relative errors $\mathcal{E}_x$, $\mathcal{E}_y$, $\mathcal{E}_\vartheta$, $\mathcal{E}_{\alpha_{-1}}$ and $\mathcal{E}_{\alpha_{+1}}$ between our theoretical prediction and the numerical integration are expected to be of the order $o(\tau^2)/\tau^2 \approx o(\tau)$, since the difference between the theoretical and numerical displacements is of order $o(\tau^2)$ while the numerical displacement itself is expected to be of order τ^2.

The approximated displacement formula employing piecewise constant controls proves effective, as demonstrated by numerical simulations. Comparisons between the displacement obtained through numerical integration, using parameters $\xi = 1$, $\eta = 2$, $\gamma = 0.1$, $\vartheta_0 = 0$, and the theoretical prediction confirm the accuracy of this approach, as shown in Figure 9.

3.3. Comparison between continuous oscillating controls and piecewise constant ones. In this section, we highlight the similarities between the solution obtained by linearising the system and applying small-amplitude oscillating controls, and the solution obtained by iterating piecewise constant controls. Importantly, for small values of γ, the controls in (3.6) can be viewed as piecewise constant approximations of the continuous controls (2.1) (see Figure 8). Indeed, for small periods, the orientation and shape trajectories converge to periodic solutions, not only with continuous controls but also with their piecewise constant approximations. Moreover, in both cases, the trajectories in the plane asymptotically result in a net translation.

For the numerical simulations, we choose $\omega = \pi/(2\tau)$, with $\tau = 0.01$. We approximate the oscillating controls (2.1) by the piecewise constant controls in (3.6) with $\gamma = \epsilon = 0.1$, (see Figure 8).

Upon integrating the equations of motion (3.1) using either the oscillating continuous controls or the piecewise constant ones, extended by periodicity in the time

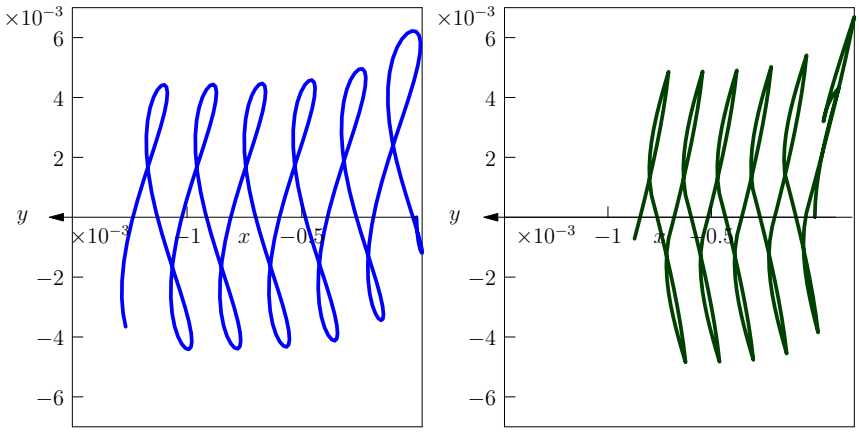

FIG. 10. *Numerical $x-y$ trajectory with continuous (left) and piecewise constant (right) inputs. Parametrs are that shown in Table 1.*

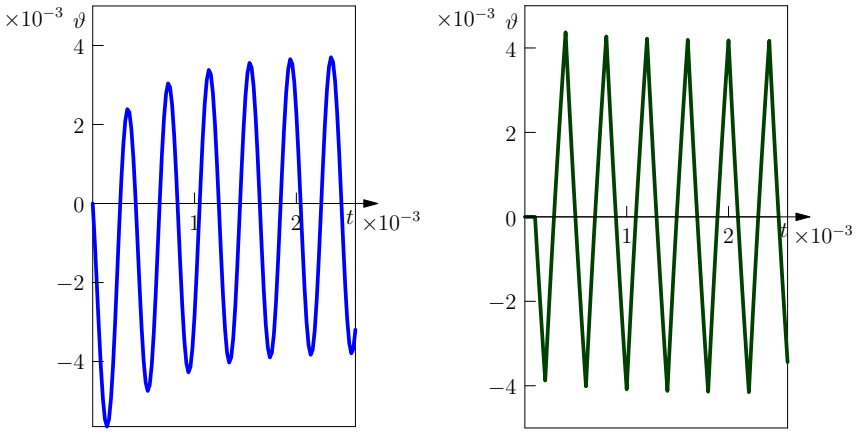

FIG. 11. *$\vartheta(t)$ with continuous (left) and piecewise constant (right) inputs. Parametrs are that shown in Table 1.*

interval $[0, 100\,\tau]$, with the initial condition $\mathbf{y}_e = (0, 0, 0, 0, 0)$, similar behaviour is observed: Figure 10 compares the $x - y$ trajectory, Figure 11 compares the variation of the orientation angle ϑ, Figure 12 compares the shape angles. Indeed, these graphs demonstrate that for both input types, both the orientation angle and the shape angles converge towards a periodic solution while the system progresses along the orientation of the central link.

3.4. Iterated theoretical displacement. In the following, we compare the evolution of the system obtained using two different methods: firstly, through numerical solution considering stepwise input gaits as defined in Equation (3.6); and secondly, by cumulating the quantities in a swimming cycle, obtained through the Lie bracket formalism (Section 3.2).

With $\gamma = 0.1$ and $\tau = 0.01$, Figure 13 presents a comparison between the theoretically predicted iterated displacement (red dots) and the numerically simulated displacement (blue dots). Similarly, comparisons for the variables $\vartheta(t)$ and $\alpha_{\mp}(t)$ are presented in Figure 14.

This manuscript is for review purposes only.

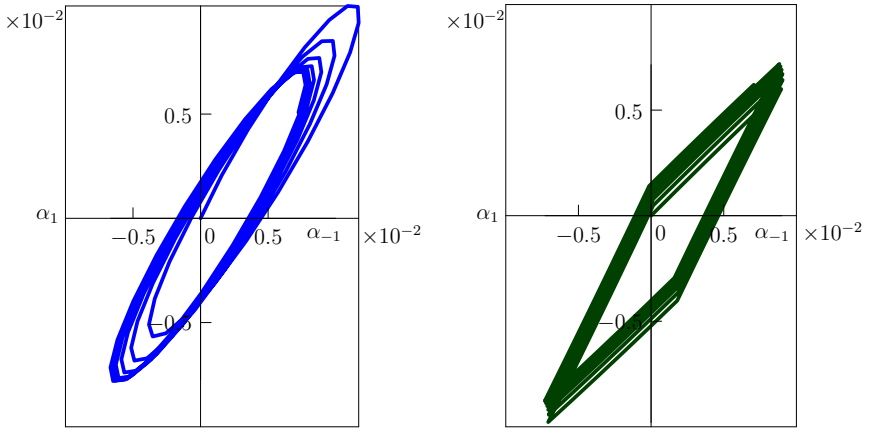

FIG. 12. $\alpha_{-1} - \alpha_{+1}$ *trajectory with continuous (left) and piecewise constant (right) inputs. Parametrs are that shown in Table 1.*

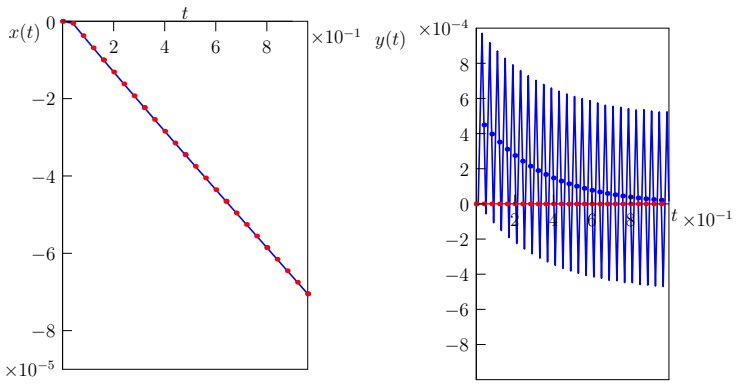

FIG. 13. *Comparison of the theoretical and numerical iterated displacements for the x-component (left) and y-component (right). Parametrs are that shown in Table 1.*

Conclusions. This study investigates the dynamics of a Purcell three-link microswimmer equipped with passive elastic torsional coils at the joints. By controlling the spontaneous curvature, effectively manipulating the equilibrium angles between the links, we aim to understand and control the swimmer's motion.

The analysis begins by linearising the system around an equilibrium point, decoupling the equations for the angular variables (describing orientation and shape) from those for the translational variables (describing the swimmer's displacement). Applying small amplitude harmonic controls to the angular subsystem, we find that it asymptotically converges to a steady harmonic solution for sufficiently long times both in the case of all links of equal length (see Figures 3 and 4) and in the case in which we consider the central link of different length (see Figures 6 and 7).

While this linear analysis provides valuable insights, it does not predict net advancement of the microswimmer. However, a subsequent weakly nonlinear analysis reveals the emergence of a translation along the orientation of the central link, both in the case of equal link lengths and in the case of unequal lengths. We analytically derive the expression for this translation in formulas (2.11) and (2.18). Furthermore, we explicitly compute the optimal frequency as a function of the ratio $\lambda = L_0/L$. The

This manuscript is for review purposes only.

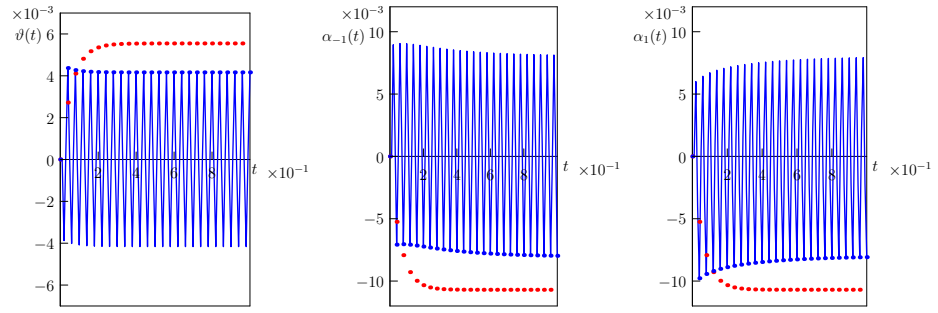

FIG. 14. *Comparison between the theoretical and numerical iterated solutions for ϑ(left), α_{-1} (centre) and α_{+1} (right). Parametrs are that shown in Table 1.*

analysis shows that the optimal frequency increases with λ, which in turn results in a higher swimming speed. This implies that when the lateral arms of the microswimmer are short compared to the central link, they oscillate at a higher frequency, thereby producing a greater displacement. Furthermore, employing tools from geometric control theory, we prove that suitable small controls can steer the system between any two fixed configurations near the equilibrium point, establishing that the system is small time locally controllable. We also provide estimates for the microswimmer's displacement, both out of equilibrium (see equation (3.7)) and at the equilibrium point (see equation (3.8)), when using piecewise constant controls.

These theoretical predictions are supported by numerical simulations, which show good agreement between the dynamics obtained using small sinusoidal controls within the linearised system and those obtained using periodic piecewise constant controls within the geometric control framework.

In conclusion, we demonstrate that our prediction of the microswimmer's displacement, derived using periodic piecewise constant controls and geometric control theory, accurately approximates the displacement achieved with small continuous oscillating controls, particularly for short time periods and over longer timescales. This suggests that other directions of motion, generated by higher-order Lie brackets, can also be achieved by combining piecewise constant controls (as defined in equation (3.6)) that generate the first-order bracket. Consequently, all directions of motion within the vicinity of the equilibrium point can be reached, at least over extended time periods, by employing suitable small oscillating controls that can be approximated by these piecewise constant controls. This conclusion is further supported by the theoretical framework established by Kurzweil and Jarník in their study on limit processes in ordinary differential equations. They rigorously demonstrate that the effects of higher-order Lie brackets can be approximated through the integration of systems subjected to rapidly oscillating inputs, thereby bridging the gap between discrete control strategies and their continuous counterparts [11]. Moreover, since we know the control inputs that generate the bracket, whether periodic or piecewise constant, we also gain constructive insight into the design of controls based on the desired behavior of the swimmer [19].

This work represents a key step towards the development of a comprehensive model for an elastic microswimmer robot, providing foundational insights into their controllability and motion planning. Future research will focus on motion planning, trajectory tracking, and optimal control problems associated with this system.

This manuscript is for review purposes only.

Acknowledgements. M.Z. and G.N. acknowledge the project "Mathematics for Industry 4.0" 2020F3NCPX PRIN2020 funded by the Italian MUR. M.Z. has been supported by the PRIN 2022 PNRR project Innovative multiscale approaches, possibly based on Fractional Calculus, for the effective constitutive modeling of cell mechanics, engineered tissues, and metamaterials in Biomedicine and related fields P2022KHFNB. All authors acknowledge support as members of the Gruppo Nazionale per la Fisica Matematica (GNFM) of the Istituto Nazionale di Alta Matematica (INdAM).

Appendix A. Entries of the $\mathcal{R}(t)$ matrix. The non-zero entries of the symmetric Grand Resistance Matrix $\mathcal{R}(t)$ are the follows, denoting as $s = \sin$ and $c = \cos$:

$$\mathcal{R}_{11} = \frac{(1-\nu)(c(2\alpha_{-1}+\vartheta)+c(2\alpha_1+\vartheta)+c(2\vartheta))-3(1+\nu)}{2\nu},$$

$$\mathcal{R}_{12} = \frac{(1-\nu)(s(2(\alpha_{-1}+\vartheta))+s(2(\alpha_{+1}+\vartheta))+s(2\vartheta))}{2\nu}$$

$$\mathcal{R}_{13} = \frac{(\nu-1)s(2\alpha_{-1}+\vartheta)-2s(\alpha_{-1}+\vartheta)+(1-\nu)s(2\alpha_{+1}+\vartheta)+2s(\alpha_{+1}+\vartheta)}{4\nu},$$

$$\mathcal{R}_{14} = -\frac{s(\alpha_{-1}+\vartheta)}{2\nu}, \qquad \mathcal{R}_{15} = \frac{s(\alpha_{+1}+\vartheta)}{2\nu}.$$

$$\mathcal{R}_{22} = -\frac{(1-\nu)(c(2(\alpha_{-1}+\vartheta))+c(2(\alpha_{+1}+\vartheta))+c(2\vartheta))+3(1+\nu)}{2\nu},$$

$$\mathcal{R}_{23} = \frac{(1-\nu)c(2\alpha_{-1}+\vartheta)+2c(\alpha_{-1}+\vartheta)+(1-\nu)c(2\alpha_{+1}+\vartheta)-2c(\alpha_{+1}+\vartheta)}{4\nu},$$

$$\mathcal{R}_{24} = \frac{c(\alpha_{-1}+\vartheta)}{2\nu}, \qquad \mathcal{R}_{25} = -\frac{c(\alpha_{+1}+\vartheta)}{2\nu}.$$

$$\mathcal{R}_{33} = \frac{c(2\alpha_{-1})(1-\nu)-4c(\alpha_{-1})-2(2c(\alpha_{+1})+4+\nu)+c(2\alpha_{+1})(\nu-1)}{8\nu},$$

$$\mathcal{R}_{34} = -\frac{3c(\alpha_{-1})+4}{12\nu}, \qquad \mathcal{R}_{35} = -\frac{3c(\alpha_{+1})+4}{12\nu}, \qquad \mathcal{R}_{44} = -\frac{1}{3\nu}, \qquad \mathcal{R}_{55} = -\frac{1}{3\nu}.$$

Appendix B. Geometric Control Theory: Fundamentals. Consider the nonlinear affine control system:

$$\dot{\mathbf{y}} = \mathbf{q}_0(\mathbf{y}) + \sum_{j=1}^{m} u_j \mathbf{q}_j(\mathbf{y}), \tag{B.1}$$

Definition 1 (Equilibrium Point). *An equilibrium point of the control system (B.1) is a pair $(\mathbf{y}_e, \mathbf{u}_e) \in \mathbb{R}^n \times \mathbb{R}^m$ such that $\mathbf{q}_0(\mathbf{y}_e) + \sum_{j=1}^{m} (\mathbf{u}_e)_j \mathbf{q}_j(\mathbf{y}_e) = 0$.*

Definition 2 (Small-Time Local Controllability). *Let $(\mathbf{y}_e, \mathbf{u}_e)$ be an equilibrium point of the control system (B.1). The system is said to be small-time locally controllable at $[\mathbf{y}_e, \mathbf{u}_e]$ if, for any $\varepsilon > 0$, there exists $\delta > 0$ such that, for every $\mathbf{y}_0 \in B_\delta(\mathbf{y}_e) = \{\mathbf{y} \in \mathbb{R}^n : |\mathbf{y} - \mathbf{y}_e| < \delta\}$ and every $\mathbf{y}_1 \in B_\delta(\mathbf{y}_e)$, there exist measurable control functions $\mathbf{u} : [0, \varepsilon] \to \mathbb{R}^m$ satisfying: $|\mathbf{u}(t) - \mathbf{u}_e| \leq \varepsilon, \quad \forall t \in [0, \varepsilon]$, and steering the system from $\mathbf{y}_0$ to $\mathbf{y}_1$ in time ε.*

This manuscript is for review purposes only.

DEFINITION 3 (Lie Algebra Rank Condition). *The control system* (B.1) *satisfies the Lie algebra rank condition at the equilibrium point* $(\mathbf{y}_e, \mathbf{u}_e)$ *if*

$$\mathcal{A}(\mathbf{y}_e, \mathbf{u}_e) = \mathbb{R}^n, \quad \textit{where} \quad \mathcal{A}(\mathbf{y}_e, \mathbf{u}_e) = \{\mathbf{g}(\mathbf{y}_e) \mid \mathbf{g} \in \textit{Lie}(\{\mathbf{q}_0, \mathbf{q}_1, \ldots, \mathbf{q}_m\})\}.$$

DEFINITION 4 (Iterated Lie Brackets). *Let* X *and* Y *be* C^∞ *vector fields on* $\mathbb{R}^n$. *The iterated Lie bracket* $ad_X^k Y$ *is defined recursively as follows:*

$$ad_X^0 Y = Y, \quad ad_X^{k+1} Y = [X, ad_X^k Y] \quad \textit{for} \quad k \in \mathbb{N}. \tag{B.2}$$

We denote by $Br(\{\mathbf{q}_0, \mathbf{q}_1, \ldots, \mathbf{q}_m\})$ *the set of formal iterated Lie brackets of* $\mathbf{q}_0, \mathbf{q}_1, \ldots, \mathbf{q}_m$. *This is the smallest subset of* $Lie(\{\mathbf{q}_0, \mathbf{q}_1, \ldots, \mathbf{q}_m\})$ *that is closed under the Lie bracket operation.*

Let $\mathbf{h}$ be a generic element of the Lie algebra generated by $\{\mathbf{q}_0, \mathbf{q}_1, \ldots, \mathbf{q}_m\}$, and let $\mathbf{h}(\mathbf{y}_e)$ be its evaluation at the equilibrium point. Note that $\mathbf{h}$ can be expressed as a linear combination of Lie brackets of various orders, where the vector fields $\mathbf{q}_j$ (with $j = 0, 1, \ldots, m$) are considered to be of order 1.

We define $\delta_j(\mathbf{h})$ as the number of times the vector field $\mathbf{q}_j$ appears in the expression for $\mathbf{h}$. For instance, for $\mathbf{h} = \mathbf{q}_1$, we have:

$$\delta_0(\mathbf{h}) = 0, \quad \delta_1(\mathbf{h}) = 1, \quad \text{and} \quad \delta_j(\mathbf{h}) = 0 \quad \text{for } j = 2, \ldots, m. \tag{B.3}$$

Similarly, for $\mathbf{h} = [\mathbf{q}_1, \mathbf{q}_2]$, we have:

$$\delta_0(\mathbf{h}) = 0, \quad \delta_1(\mathbf{h}) = 1, \quad \delta_2(\mathbf{h}) = 1, \quad \text{and} \quad \delta_j(\mathbf{h}) = 0 \quad \text{for } j = 3, \ldots, m. \tag{B.4}$$

Let $\mathfrak{S}_m$ be the symmetric group on $\{1, \ldots, m\}$. For each permutation $\pi \in \mathfrak{S}_m$, let $\tilde{\pi}$ denote the automorphism of $\mathrm{Lie}(\{\mathbf{q}_0, \ldots, \mathbf{q}_m\})$ defined by $\tilde{\pi}(\mathbf{q}_0) = \mathbf{q}_0$ and $\tilde{\pi}(\mathbf{q}_i) = \mathbf{q}_{\pi(i)}$ for $i = 1, \ldots, m$.

For $\mathbf{h} \in \mathrm{Br}(\{\mathbf{q}_0, \mathbf{q}_1, \ldots, \mathbf{q}_m\})$, we define

$$\sigma(\mathbf{h}) := \sum_{\pi \in \mathfrak{S}_m} \tilde{\pi}(\mathbf{h}) \in \mathrm{Lie}(\{\mathbf{q}_0, \ldots, \mathbf{q}_m\}).$$

For instance, when $m = 2$, we have

$$\sigma(\mathbf{h}) = \mathbf{h} + \tilde{\pi}(\mathbf{h}) = [\mathbf{q}_1, \mathbf{q}_2] + [\mathbf{q}_2, \mathbf{q}_1].$$

DEFINITION 5 (Sussmann Condition). *For* $\Lambda \in [0, +\infty]$, *the control system* (B.1) *satisfies the Sussmann condition* $S(\Lambda)$ *if:*

1. *The Lie algebra rank condition (LARC) in Definition 3 holds at the equilibrium* $(\mathbf{y}_e, \mathbf{u}_e)$.
2. *For every* $\mathbf{h} \in Br(\{\mathbf{q}_0, \mathbf{q}_1, \ldots, \mathbf{q}_m\})$ *with* $\delta_0(\mathbf{h})$ *odd and* $\delta_i(\mathbf{h})$ *even for* $i = 1, \ldots, m$, $\sigma(\mathbf{h})(\mathbf{y}_e)$ *lies in the span of the* $\mathbf{g}(\mathbf{y}_e)$*'s, where the* $\mathbf{g}$*'s are elements of* $Br(\{\mathbf{q}_0, \mathbf{q}_1, \ldots, \mathbf{q}_m\})$ *and satisfy:*

$$\Lambda \delta_0(\mathbf{g}) + \sum_{k=1}^{m} \delta_k(\mathbf{g}) < \Lambda \delta_0(\mathbf{h}) + \sum_{k=1}^{m} \delta_k(\mathbf{h}),$$

with the convention that, when $\Lambda = +\infty$, *the inequality becomes* $\delta_0(\mathbf{g}) < \delta_0(\mathbf{h})$.

This manuscript is for review purposes only.

THEOREM B.1. *If, for some* $\Lambda \in [0,1]$*, the control system* (B.1) *satisfies the Sussmann condition, then it is small-time locally controllable.*

REFERENCES

[1] F. ALOUGES, A. DESIMONE, L. GIRALDI, AND M. ZOPPELLO, *Can magnetic multilayers propel artificial microswimmers mimicking sperm cells?*, Soft Robotics, 2 (2015), pp. 117–128.

[2] F. ALOUGES, A. DESIMONE, L. GIRALDI, AND M. ZOPPELLO, *Purcell magneto-elastic swimmer controlled by an external magnetic field*, IFAC-PapersOnLine, 50 (2017), pp. 4120–4125.

[3] R. ATTANASI, M. ZOPPELLO, AND G. NAPOLI, *Purcell's swimmers in pairs*, Physical Review E, 109 (2024), p. 024601.

[4] F. BAGAGIOLO, R. MAGGISTRO, AND M. ZOPPELLO, *Swimming by switching*, Meccanica, 52 (2017), pp. 3499–3511.

[5] A. S. BOIARDI AND G. NOSELLI, *Minimal actuation and control of a soft hydrogel swimmer from flutter instability*, Journal of the Mechanics and Physics of Solids, 191 (2024), p. 105753, https://doi.org/https://doi.org/10.1016/j.jmps.2024.105753, https://www.sciencedirect.com/science/article/pii/S0022509624002199.

[6] J.-M. CORON, *Control and Nonlinearity*, no. 136 in Mathematical Surveys and Monographs, American Mathematical Society, 2007.

[7] Y. EL ALAOUI-FARIS, J.-B. POMET, S. RÉGNIER, AND L. GIRALDI, *Optimal actuation of flagellar magnetic microswimmers*, Phys. Rev. E, 101 (2020), p. 042604, https://doi.org/10.1103/PhysRevE.101.042604, https://link.aps.org/doi/10.1103/PhysRevE.101.042604.

[8] J. ELGETI, R. G. WINKLER, AND G. GOMPPER, *Physics of microswimmers—single particle motion and collective behavior: a review*, Reports on progress in physics, 78 (2015), p. 056601.

[9] J. GRAY AND G. HANCOCK, *The propulsion of sea-urchin spermatozoa*, Journal of Experimental Biology, 32 (1955), pp. 802–814.

[10] J. GRAY AND G. J. HANCOCK, *The propulsion of sea-urchin spermatozoa*, Journal of Experimental Biology, 32 (1955), pp. 802–814.

[11] J. KURZWEIL AND J. JARNÍK, *Limit processes in ordinary differential equations*, Zeitschrift für angewandte Mathematik und Physik ZAMP, 38 (1987), pp. 241–256.

[12] E. LAUGA, *Floppy swimming: Viscous locomotion of actuated elastica*, Phys. Rev. E, 75 (2007), p. 041916, https://doi.org/10.1103/PhysRevE.75.041916, https://link.aps.org/doi/10.1103/PhysRevE.75.041916.

[13] R. MARCHELLO, M. MORANDOTTI, H. SHUM, AND M. ZOPPELLO, *The n-link swimmer in three dimensions: Controllability and optimality results*, Acta Applicandae Mathematicae, 178 (2022), p. 6.

[14] C. MOREAU, L. GIRALDI, AND H. GADÊLHA, *The asymptotic coarse-graining formulation of slender-rods, bio-filaments and flagella*, Journal of the Royal Society Interface, 15 (2018), p. 20180235.

[15] A. OULMAS, N. ANDREFF, AND S. RÉGNIER, *3d closed-loop motion control of swimmer with flexible flagella at low reynolds numbers*, in 2017 IEEE/RSJ International Conference on Intelligent Robots and Systems (IROS), 2017, pp. 1877–1882, https://doi.org/10.1109/IROS.2017.8206004.

[16] E. PASSOV AND Y. OR, *Dynamics of Purcell's three-link microswimmer with a passive elastic tail*, The European Physical Journal E, 35 (2012), pp. 1–9.

[17] K. E. PEYER, L. ZHANG, AND B. J. NELSON, *Bio-inspired magnetic swimming microrobots for biomedical applications*, Nanoscale, 5 (2013), pp. 1259–1272.

[18] E. M. PURCELL, *Life at low reynolds number*, American Journal of Physics, 45 (1977), pp. 3–11.

[19] H. SHUM, M. ZOPPELLO, M. ASTWOOD, AND M. MORANDOTTI, *Control of microparticles through hydrodynamic interactions*, Journal of Fluid Mechanics, 1004 (2025), p. A4.

[20] Z. YE, S. RÉGNIER, AND M. SITTI, *Rotating magnetic miniature swimming robots with multiple flexible flagella*, IEEE Transactions on Robotics, 30 (2014), pp. 3–13, https://doi.org/10.1109/TRO.2013.2280058.

[21] A. ZIGELMAN, G. BEN ZVI, AND Y. OR, *Dynamics of purcell-type microswimmers with active-elastic joints*, Phys. Rev. E, 110 (2024), p. 014207, https://doi.org/10.1103/PhysRevE.110.014207, https://link.aps.org/doi/10.1103/PhysRevE.110.014207.

[22] M. ZOPPELLO, M. MORANDOTTI, AND H. BLOOMFIELD-GADÊLHA, *Controlling non-controllable scallops*, Meccanica, 57 (2022), pp. 2187–2197.

This manuscript is for review purposes only.